Full Length Article

Unveiling the shape-selective CoCr$_{2-y}$Sc$_y$O$_4$ nanomagnetism

V. Jagadeesha Angadi [a,b], K. Manjunatha [c], Marisa C. Oliveira [d], Elson Longo [d], Sergio R. de Lázaro [e], Renan A.P. Ribeiro [f,*], S.V. Bhat [a,*]

[a] Department of Physics, Indian Institute of Science, Bangalore 560012, India
[b] Department of Physics, P.C. Jabin Science College, Hubballi 580031, India
[c] Department of Physics, School of Engineering, Presidency University, Bangalore 560064, India
[d] Center for the Development of Functional Materials (CDMF), Federal University of São Carlos, São Carlos, SP, Brazil
[e] Department of Chemistry, State University of Ponta Grossa, Ponta Grossa, PR, Brazil
[f] Department of Chemistry, Minas Gerais State University, Divinópolis, MG, Brazil

ARTICLE INFO

ABSTRACT

In this study CoCr$_{2-y}$Sc$_y$O$_4$ (y = 0, 0.01, 0.02, and 0.03) nanoparticles (NPs) have been synthesized following the solution combustion method and characterized by combining experimental techniques with high-throughput Density Functional Theory calculations. The structural analysis confirmed the crystalline nature with spinel cubic structure exhibiting an average particle size between 7 and 10 nm. The morphological analysis confirmed the exposure of the (220), (311), (400), and (422) planes in agreement with theoretical results based on Wulff Construction. Magnetic analysis indicated the existence of paramagnetic to ferrimagnetic phase transition at the critical temperature (T$_c$) and a conical spiral spin phase was found at the spiral transition temperature (T$_s$). In both the cases, the transition temperature was seen to decrease with increase in the Sc content in agreement with the exchange-coupling constants calculated by DFT, where a singular magneto-structural behavior was observed. Theoretical results for shape-oriented magnetic properties indicate the anisotropic spin density distribution and surface exposure, providing a general picture of shape-selective control of nanomagnetism.

1. Introduction

Spinel chromites with the general formula ACr$_2$O$_4$ have received good scientific attention due to their promising applications in diverse areas such as in electrochemical sensors, biomedical materials, catalysis, spintronics, magnetic resonance imaging, and high-temperature ceramics [1–4]. They are also investigated for their interesting properties [5–7]. In these compounds, the magnetic and ferroelectric properties coexist and the magnetic properties can be controlled by electric field and vice versa thus making them technologically significant for switching devices, random access memories, and magnetoelectric memories [8].

Cobalt chromite (CoCr$_2$O$_4$) is a ferrimagnetic material having a spinel structure with space group *Fd-3m* [9]. It is a normal spinel where Co^{2+} ions occupy the A sites and Cr^{3+} ions occupy the B sites of the spinel structure. [10]. The CoCr$_2$O$_4$ nanoparticles (NPs) exhibit long-range ferrimagnetic order below the critical temperature (T$_c$) and non-collinear conical spiral spin order at a spiral transition temperature (T$_s$) [11,12]. At low temperatures, cobalt chromite NPs show interesting

behaviour in their magnetic properties. Zakutna et al. [13] reported a size-based glassy-like state in CoCr$_2$O$_4$ NPs. Rathi et al. [14] observed a spin-glass structure in NiCr$_2$O$_4$ NPs resulting from interactions among surface and ordered core spins. However, Mohanty et al. [12,15] observed that the position of the ac-susceptibility peak of CoCr$_2$O$_4$ NPs did not change with frequency, ruling out the possibility of a spin-glass-like structure in the sample. Rath et al. [16,17] studied the transitions in CoCr$_2$O$_4$ NPs and found an intermediate superparamagnetic phase between Tc and the blocking temperature which was somewhat higher than Ts. They attributed this behavior to disordered spin configuration at the surfaces and the distribution of NP sizes. Ptak et al. [18] in their magnetic and IR studies of CoCr$_2$O$_4$ NPs found the evidence for the development of an incommensurate phase below T$_s$ and also for spin phonon coupling. Tian et al. [19] found a decrease in both T$_c$ and T$_s$ in CoCr$_2$O$_4$ NPs which they attribute to the spin disorder produced at the surface of the NPs. Chen et al. [20] observed that in CoCr$_2$O$_4$, commensurate and incommensurate spiral orders coexist. With application of high pressure they found a rise in T$_s$ and lock-in transition temperature (T$_l$) caused by lattice contraction leading to more

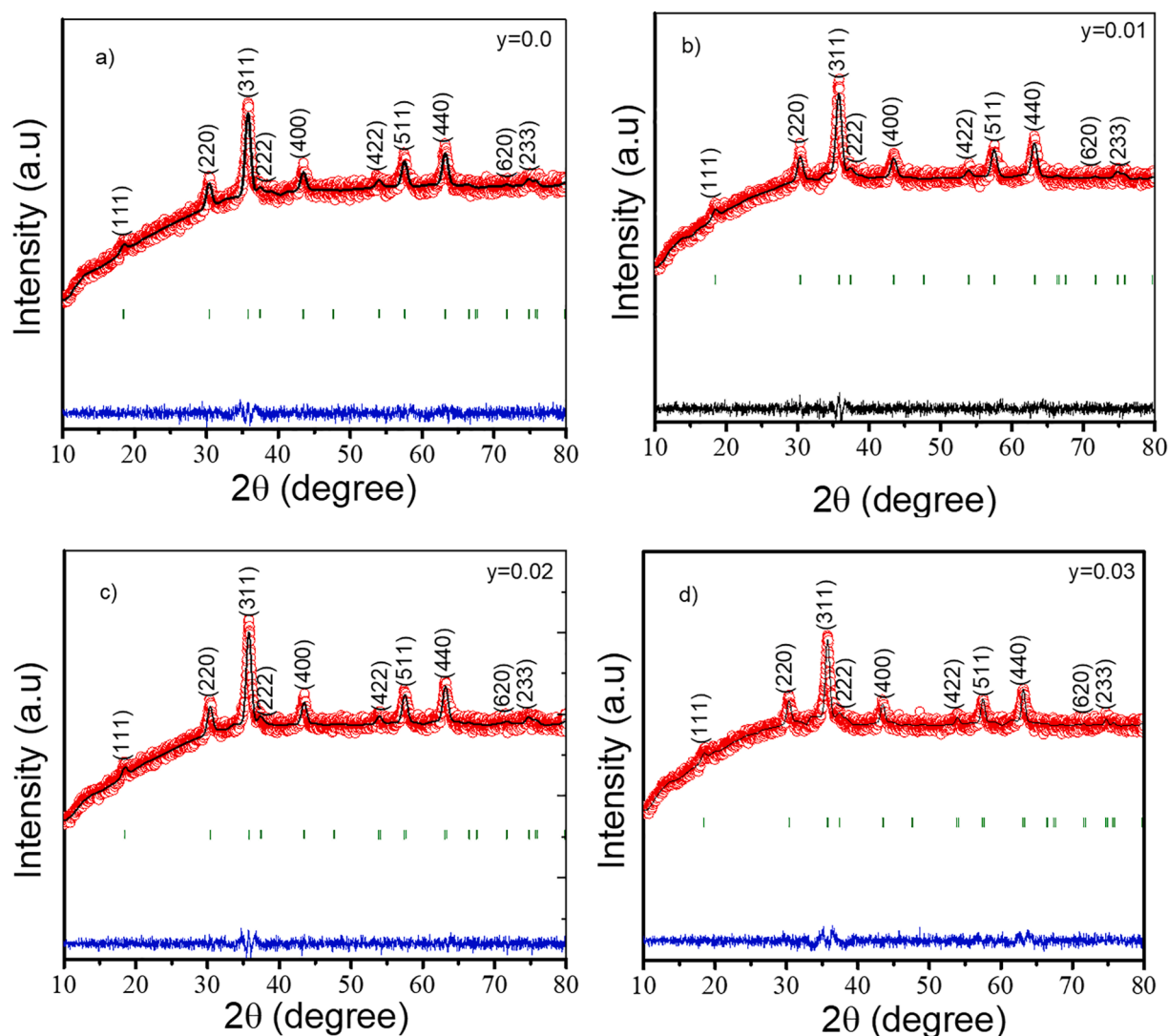**Fig. 1.** Rietveld refined XRD patterns of the as-synthesized $CoCr_{2-y}Sc_yO_4$ for a) y = 0.0, b) 0.01, c) y = 0.02 and d) y = 0.03.

Table 1
Experimental values for lattice parameter, crystallite size (diameter) and Rietveld refinement parameters (R_p, R_{wp}, R_{exp} and χ^2) of $CoCr_{2-y}Sc_yO_4$ (y = 0, 0.01, 0.02 and 0.03) samples.

Sc^{3+} content	Lattice parameter (Å)	Crystallite size (nm)	R_p	R_{wp}	R_{exp}	χ^2
y = 0	8.3229	10	1.52	1.90	1.78	1.15
y = 0.01	8.3259	9.5	1.41	1.78	1.66	1.14
y = 0.02	8.3276	10	1.42	1.79	1.71	1.10
y = 0.03	8.3294	9.6	1.48	1.88	1.72	1.20

significant magnetic frustration.

Control of $CoCr_2O_4$ magnetic properties through site-selective doping i.e., doping in either tetrahedral or octahedral sites from the point of view of technological applications is currently an active area of research [5,9,21–31]. We have recently studied the effects of the Bi- and Sc-doping in $CoCr_2O_4$ NPs, providing compelling evidence that tetrahedral site doping modifies exchange coupling strength between Co-Co, Co-Cr, and Cr-Cr resulting in singular magneto-structural behavior [32,33]. Motivated by the literature referred to above, herein, the structural, microstructural, and magnetic behaviors of $CoCr_{2-y}Sc_yO_4$ (y = 0, 0.01, 0.02, and 0.03) NPs are investigated through a combined experimental-theoretical study.

2. Experimental

2.1. Sample preparation

Stoichiometric amounts of metal nitrates like cobaltous nitrate, scandium nitrate, and chromium nitrate, as well as fuels like glucose and urea (details in *Supporting Information*), were dissolved in distilled water in a glass beaker and stirred for one hour with a magnetic stirrer to obtain a homogeneous solution. The solution was heated at 450 °C in a preheated box-type muffle furnace. The fluid initially boiled, frothed, and then ignited. Within 20 min, the combustion process was completed. The resulting material was crushed into a fine powder with an agate mortar and pestle.
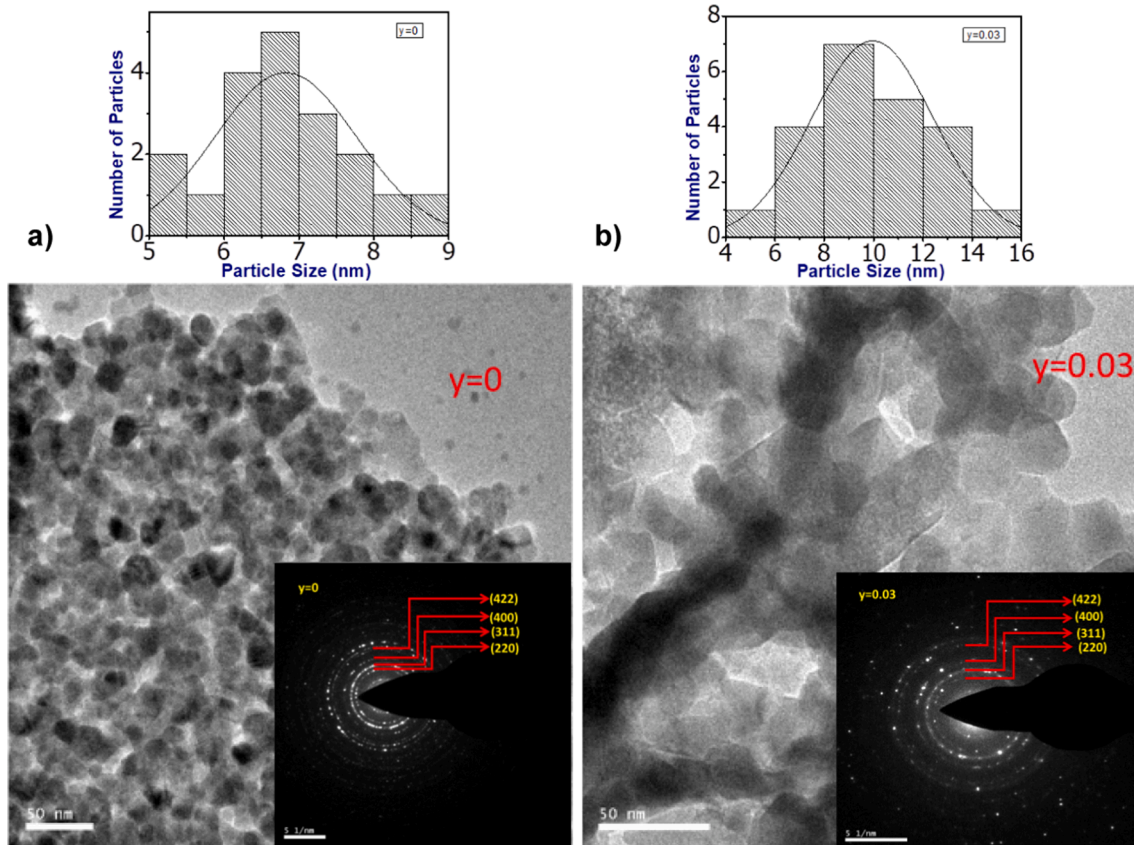
Fig. 2. TEM images, Particle size distribution histograms and SAED patterns of CoCr$_{2-y}$Sc$_y$O$_4$ NPs with a) y = 0.0 and b) y = 0.03.

2.2. Sample characterization

X-ray diffraction (XRD) patterns of the samples were recorded using a 'PANalytical X-ray diffractometer' with Cu-K radiation (λ = 1.54056 Å) in the 2θ range of 10-80° with a step size of 0.02°. Rietveld refinement of the patterns was carried out using the FULLPROF software to obtain the crystal structure parameters. Scherrer formula was used to determine the particle size. As regard the analysis of Sc-content, it is important to mention that only stoichiometric estimative were considered (details in *Supporting Information*), once elemental-based analysis were not available due to the COVID-19 pandemic. Transmission electron microscopy (TEM) images and selective area electron diffraction (SAED) patterns were recorded on a Philips (JEM-2100 TEM) instrument. The samples were examined under this TEM after dispersing the sample in ethyl alcohol and placing it on a copper grid. TEM generates the high-resolution image of lattice structure of the crystalline material which gives the direct characterization of the sample's atomic structure. Further, the particle size distribution of the samples was estimated by using ImageJ software. The magnetization investigations were performed by using a SQUID magnetometer at 500 Oe field in the temperature range from 2 to 400 K. The susceptibility (χ) was calculated by using $\chi = \frac{M}{H}$, where M is the measured magnetization and H is the applied field. The field dependent magnetization (M−H loops) was studied by using the SQUID magnetometer at three different temperatures (10, 95, and 300 K) in the field range ± 20,000 Oe.

2.3. Density functional theory calculations

CRYSTAL17 [34] was used to perform density functional theory calculations utilizing the non-empirical PBE0 hybrid functional [35]. The electronic structure of oxide materials is well described by hybrid exchange–correlation functionals (B3PW, PBE0, and B3LYP) [36,37], with PBE0 being the most trustworthy choice for multiferroic materials [38].

The supercell expansion (112-atoms) was used to create theoretical models for CoCr$_2$O$_4$ and CoCr$_{2-y}$Sc$_y$O$_4$ models. In addition, the isoelectronic substitution of Cr^{3+} by Sc^{3+} was studied for Sc-doped models.

Three Ferrimagnetic (FiM) collinear models were used to determine the exchange-coupling constant compared to Ferromagnetic orientation (FEM). Herein, the primitive CoCr$_2$O$_4$ cell comprising 14-atoms can be used to describe the magnetic orientation once two Co and four Cr atoms are surrounded by eight O atoms, resulting in a FEM model (Co$_{\uparrow\uparrow}$Cr$_{\uparrow\uparrow\uparrow\uparrow}$). The FiM-1, FiM-2, and FiM-3 were described as (Co$_{\downarrow\downarrow}$Cr$_{\uparrow\uparrow\uparrow\uparrow}$), (Co$_{\uparrow\downarrow}Cr_{\uparrow\uparrow\uparrow\uparrow}$), and (Co$_{\uparrow\uparrow}Cr_{\uparrow\downarrow\uparrow\downarrow}$), respectively. [33] The Ising model estimated the exchange-coupling constant (J) based number of atom neighbors i–j (Z) and the electronic spin of different species (S):

$$\widehat{H}_{ising} = \sum J_{ij} \widehat{S}_{iz} \widehat{S}_{jz} \qquad (1)$$

$$\Delta E_{FIM-FEM} = -2 \sum Z_{ij} S_i S_j J_{ij} \qquad (2)$$

Moreover, the (1 0 0), (1 1 0), (1 1 1), and (3 1 1) surfaces for CoCr$_{2-y}$Sc$_y$O$_4$ were modeled combining a thermodynamic method with spin density analysis, as reported in earlier studies [32,39–49].

The lattice parameters and atomic locations were relaxed for all models. The reciprocal space based on the Monkhorst-Pack approach for bulk (surface) models was represented using 8 × 8 × 8 (4 × 4 × 4) shrinkage factors, which was a suitable mesh to explain the electrical and energetic characteristics [50]. Co, Cr, and O atoms were characterized using an all-electron basis set [51–53], while Sc centers were described using an effective-core pseudopotential [54].
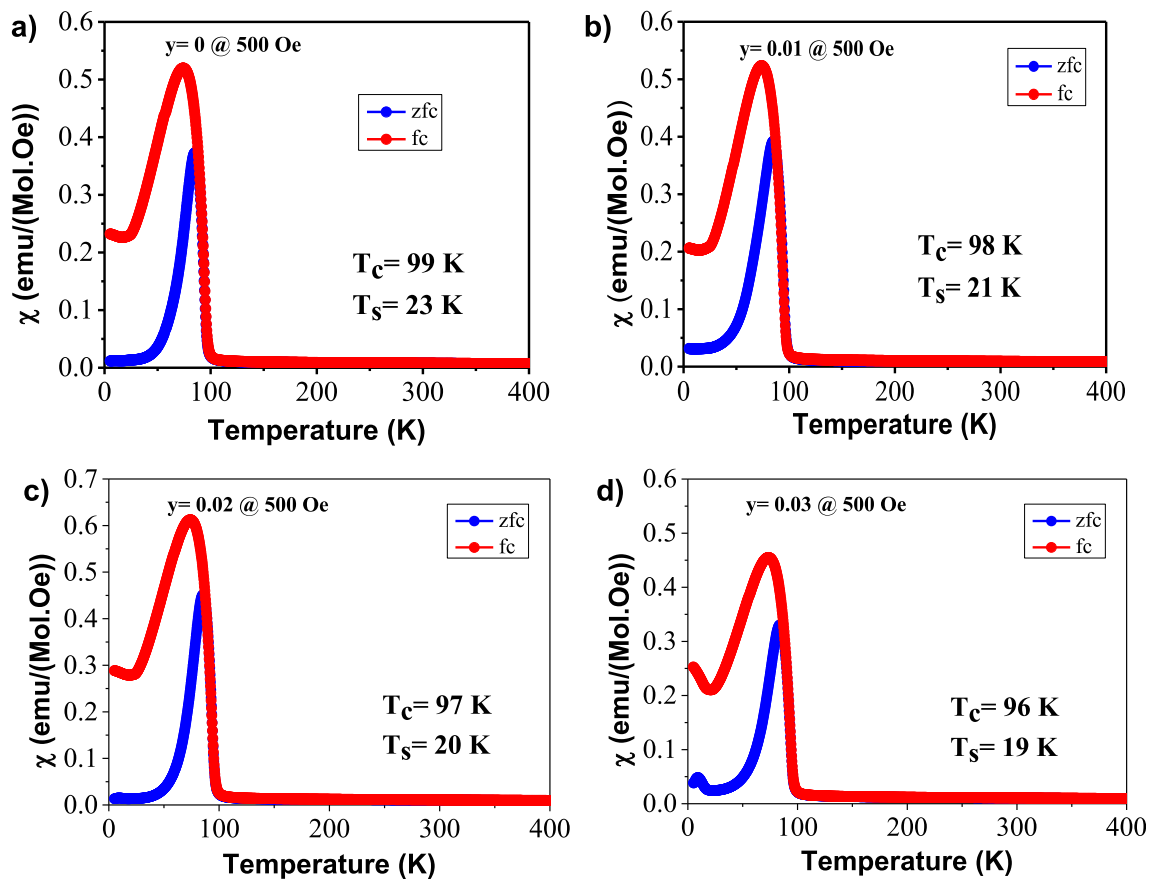
Fig. 3. Temperature dependent susceptibility χ(T) of CoCr$_{2-y}$Sc$_y$O$_4$ for a) y = 0, b) y = 0.01, c) y = 0.02 and d) y = 0.03 NPs.

3. Results and discussion

3.1. Structural analysis

The XRD patterns for the as-synthesized CoCr$_{2-y}$Sc$_y$O$_4$ (y = 0, 0.01, 0.02 and 0.03) samples are shown in Fig. 1. The patterns are characteristic of a single phase with a spinel cubic structure and the patterns match well with JCPDS file no. 780711 [33]. The figure also shows the results of Rietveld refinement carried out using the FULLPROF software. During the refinement the crystal structure and profile parameters such as lattice constants, atomic coordinates, occupancy of the ions, isotropic temperature factors, background corrections, peak shape parameters, symmetry and asymmetric parameters were refined so that the difference between the observed experimental XRD data and the calculated diffraction patterns was minimized by using least squares procedure. The results of the refinement are presented in Table 1 which lists the structural characteristics, phase composition and Rietveld refinement parameters (R$_p$, R$_{wp}$, R$_{exp}$ and χ^2). The average crystallite size (diameter D) was estimated by using Scherrer method. D was calculated from the widths of diffraction peaks using the Scherrer equation (3)

$$D = \frac{0.9\lambda}{\beta cos\theta} nm \tag{3}$$

where λ is the X-ray wavelength (in our experiment λ = 1.54056 Å), β is the diffraction peak full width at half maximum (in radians), θ is the angle of diffraction, and 0.9 is the Scherrer constant. Using this method, we calculated the mean size of crystallites from the width of the [311] peak at 2θ = 35.71. Table 1 also summarizes the crystallite size values along with the lattice characteristics. It is seen that the lattice parameter increases as Sc^{3+} concentration increases. This is as expected because Sc^{3+} ions have a higher ionic radius (0.745 Å) than that of the Cr^{3+} ions

(0.52 Å).

3.2. Morphological analysis

TEM images, particle size distribution histograms, and Selected Area Electron Diffraction (SAED) patterns of CoCr$_{2-y}$Sc$_y$O$_4$ samples with y = 0.0 and 0.03 are shown in Fig. 2, indicating a non-uniform shape for pure samples that becomes more faceted with the Sc-doping. The average particle size is 7 nm and 10 nm for y = 0 and y = 0.03, respectively. These values are well-matched with the average crystallite sizes calculated from the X-ray diffraction, showing the polycrystalline nature of the particles. The spotty ring patterns identified with the (220), (311), (400), and (422) planes from SAED confirm the crystallinity of the NPs.

3.3. Magnetic analysis

Fig. 3 shows the temperature-dependent susceptibility χ(T) of CoCr$_{2-y}$Sc$_y$O$_4$ (y = 0, 0.01, 0.02, and 0.03) obtained from magnetization measurements carried out in zero-field cooled and field cooled conditions at an applied magnetic field of 500 Oe. In all cases, the samples were warmed to 400 K to ensure that the sample regained the paramagnetic phase.

All the samples showed a rapid increase of FC and ZFC susceptibilities at a specific temperature (i.e., the critical temperature, T$_c$) on decreasing the temperature from 400 K, indicating the paramagnetic to a long-range ferrimagnetic phase transition. The T$_c$ values were obtained as 99 K, 98 K, 97 K, and 96 K for y = 0, 0.01, 0.02, and 0.03, respectively, which are close to the data obtained by Tomiyasu et al. [55] for CoCr$_2$O$_4$ single crystal and by Pronin et al. [56] for polycrystalline CoCr$_2$O$_4$.

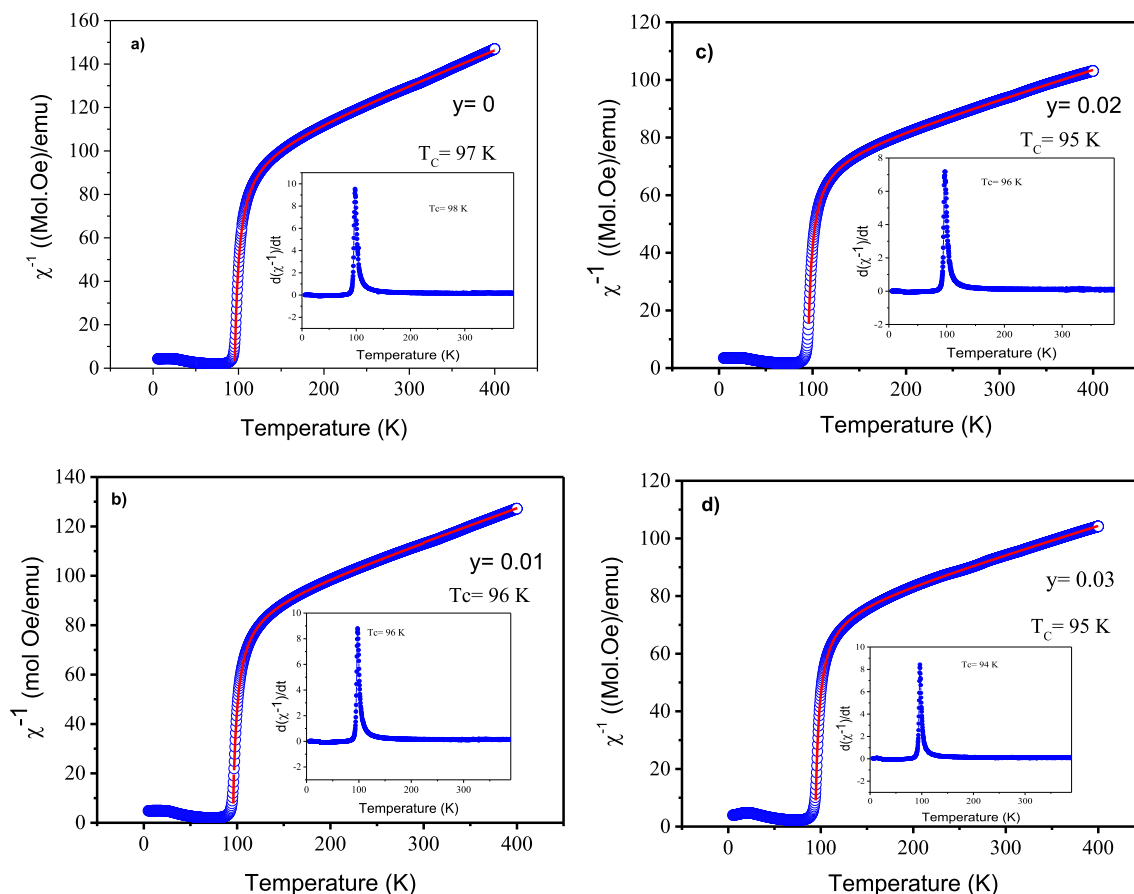Below the critical temperature, as the temperature decreases, the FC

Fig. 4. Temperature dependence of reciprocal susceptibility of FC magnetization and its derivative (inset) for $CoCr_{2-y}Sc_yO_4$ a) y = 0, b) y = 0.01, c) y = 0.02 and d) y = 0.03 NPs.

curve shows an anomaly associated with the conical spin-spiral order phase, i.e., spiral transition temperature (T_s). The T_s values were found to be 23 K, 21 K, 20 K and 19 K for y = 0, 0.01, 0.02 and 0.03, respectively.

To understand the critical behavior of the samples, we adopted equation (4) containing a Curie-Weiss (ferrimagnetic) term and a Curie (paramagnetic) term to fit the temperature-dependent reciprocal of susceptibility $\chi^{-1}(T)$ as shown in Fig. 4:

$$\chi^{-1}(T) = \left(\frac{T}{C} + \frac{1}{\xi}\right) - \left(\frac{b}{T - \Theta'}\right) \tag{4}$$

where χ^{-1} is the reciprocal susceptibility, C is the Curie constant, T is the temperature, ξ, Θ' and b are constants [9]. The paramagnetic term's presence is related to the no saturation behavior exhibited by chromites [57]. The high-temperature experimental data (paramagnetic) is well fitted by equation (4) with a deviation happening close to the Curie temperature. The obtained theoretical values for critical temperatures are $T_c \sim 97$, 96, 95, and 95 K for y = 0, 0.01, 0.02, and 0.03, respectively, showing an excellent agreement with the experimental results. In spinels, the critical temperature (T_c) is controlled by the exchange interaction between ions at the tetrahedral and octahedral sites. Therefore, the observed decrease in the critical temperature with the increase of Sc^{3+} concentration suggests that the exchange interaction between the tetrahedral and octahedral sites weakens because of substitution of Cr^{3+} ions by Sc^{3+} ions in the octahedral site. Our results on Sc-doped $CoCr_2O_4$ nanoparticles show that both T_c and T_s decrease as the Sc concentration increases. One possible reason for this could be the random distribution of Sc^{3+} ions at the tetrahedral and octahedral sites. The structural analysis, on the other hand, confirmed that the lattice

parameter increases with increasing Sc concentration. As a result, the weakening of the magnetic transition at the spiral transition temperature in Sc doped $CoCr_2O_4$ nanoparticles is a result of an intrinsic change in noncollinear to collinear spin structure of B sites in $CoCr_2O_4$, and following [58] it is directly related to the system's lattice disorder. The lattice disorder in Sc doped $CoCr_2O_4$ nanoparticles leads to a decrease in B site direct interactions which results in a change in B site spin structure from noncollinear to collinear.

Further, the magnetization as a function of applied magnetic field at different temperatures was investigated, as shown in Fig. 5. For all samples, the linear magnetization dependence at 300 K confirms the paramagnetic nature [59]. An apparent hysteresis loop appears at 10 K, with the coercivity (H_c) and remnant magnetization (M_r), which can be associated with the ferrimagnetic behavior of $CoCr_2O_4$. The remnant magnetization is found to be 0.3599 emu/g, 0.1578 emu/g and 0.0977 emu/g for y = 0, 0.02 and 0.03 concentration, respectively. The coercivity is found to be 3912 Oe, 2581 Oe, and 956 Oe for y = 0, 0.02, and 0.03 concentrations, respectively. The magnetization vs. magnetic field curve shows a hysteresis loop also at 95 K temperature, indicating the ferrimagnetic nature of Sc^{3+} doped $CoCr_2O_4$ NPs at these temperatures.

3.4. Theoretical analysis

The results of DFT calculations for $CoCr_{2-y}Sc_yO_4$ bulk and surface models, concentrating on structural, electrical, and magnetic characteristics, are provided in this section. Following the experimental investigation, the optimal lattice parameters for pure $CoCr_2O_4$ and Sc-doped models were estimated as $a = 8.375$ and $a = 8.423$, respectively, suggesting a unit cell expansion (Table 1). The M—O bond lengths accompany such volume expansion (Table S2 - Supporting
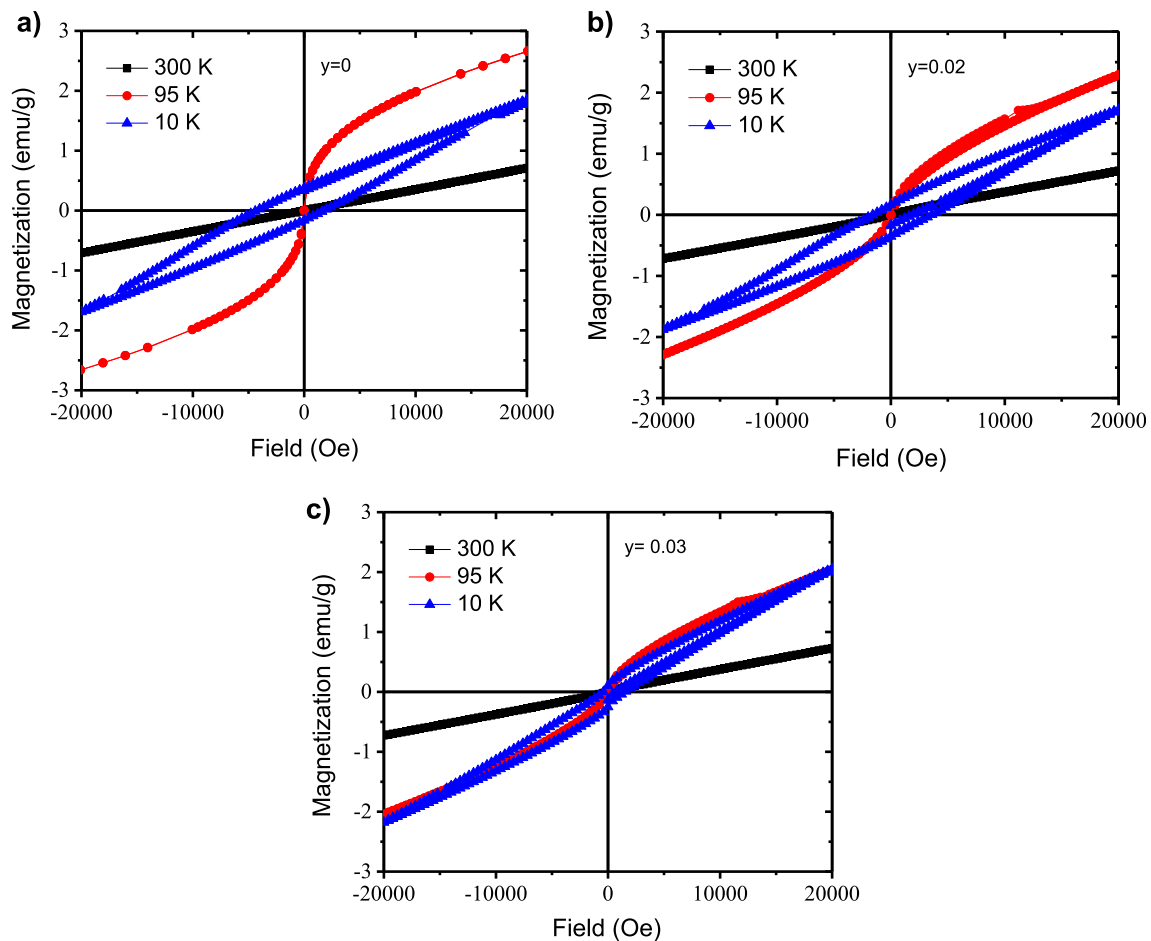
Fig. 5. Field dependent magnetization at 300 K, 95 K and 10 K for $CoCr_{2-y}Sc_yO_4$ a) y = 0, b) y = 0.02 and c) y = 0.03 NPs.

Table 2
Exchange coupling constants calculated for both pure and Sc-doped $CoCr_2O_4$ models.

	$CoCr_2O_4$	$CoCr_{2-y}Sc_yO_4$	$Co_{1-x}Sc_xCr_2O_4$ [a]
J_{Co-Co}	−57.51	−99.11	−50.53
J_{Cr-Cr}	−46.41	−73.19	−74.05
J_{Co-Cr}	−32.55	−55.98	−50.27
$u = 4J_{BB}S_B/3J_{AB}S_A$	2.07	1.91	2.10

[a] Ref. [33].

Information), where it was visualized the local structural disorder in the B-site of $CoCr_2O_4$, resulting in larger Sc-O bonding paths that spread along with the entire crystalline structure, inducing some larger Co-O and Cr-O bond distances closer to the doping site.

The exchange coupling constants were used to examine the bulk magnetic characteristics of $CoCr_{2-y}Sc_yO_4$, as reported in Table 2.

As a result, we may claim that Sc doping in conjunction with the A- or B-sites of $CoCr_2O_4$ causes structural disorders that control exchange-coupling interactions. The B-site doping is the most advantageous mechanism for inducing a multiple AFM environment for all magnetic interactions. This fact is demonstrated by comparing the computed exchange-coupling constant to the T_c values provided in the preceding section.

Therefore, we can argue that Sc doping and A- or B-site of $CoCr_2O_4$ induce structural disorders that govern the exchange-coupling interactions. The B-site doping is the most favorable mechanism to induce several AFM environments for all magnetic interactions. This fact can be proved by comparing the calculated exchange-coupling constant with the T_c values reported in the previous section. Herein, increasing the

AFM extent for all A-A, A-B, and B-B magnetic interaction, the T_c values decrease with the Sc-content once the ferrimagnetic ordering resulting from dominant J_{Co-Co} interactions becomes smaller due to the increased contribution of J_{Co-Cr}. In a Ferrimagnetic Neel model, the A and B-site cations are antiparallelly ordered; however, increasing the role of J_{Co-Cr}, the ferromagnetic ordering becomes more unstable.

The LKDM model [60] can describe a cubic-spinel compound's magnetic ground state and magnetic frustration. The estimated u values for pure and Sc-doped $CoCr_2O_4$ models suggest that the spiral state exists; nevertheless, it is unstable from the LKDM model's bases.

Let us examine the electronic structure of $CoCr_{2-y}Sc_yO_4$ using the FiM-1 Neel model, as shown in Fig. 6. The band-gap region of pure $CoCr_2O_4$ (Fig. 6a) exhibits a band-gap of 4.77 eV (X-X) for the majority spin-channel involving the Cr and Co (3d) orbitals hybridized with O (2p) states. Furthermore, the electron density redistribution for the Sc-doped model (Fig. 6b) reduces the band-gap to 4.63 eV (Γ-Γ).

Compared with our previous study for A-site Sc doping [41], the B-site cation doping contribution for band-gap narrowing is small, associated with the isoelectronic replacement of Cr^{3+} by Sc^{3+} not requiring
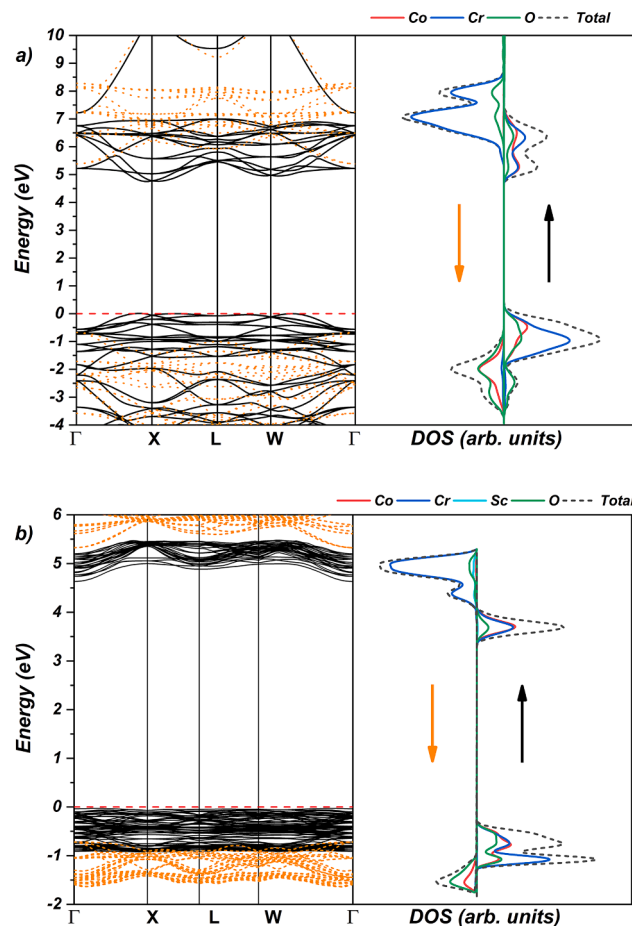
Fig. 6. Theoretical results for Density of States and Band Structure profiles for (a) $CoCr_2O_4$ and (b) $CoCr_{2-y}Sc_yO_4$ models.

the creation of neighboring vacant sites to maintain the supercell neutrality. This fact is an interesting contribution that can guide future studies for doped $CoCr_2O_4$ regarding the electronic properties once the A-site cation doping induces a higher electronic structure disorder with intermediary energy levels from vacant sites than B-site doping.

Despite the essential features reported for bulk models, the precise understanding of surface magnetism is a crucial step in developing multifunctional nanomagnetism. Herein, the $(1\,0\,0)$, $(1\,1\,0)$, $(1\,1\,1)$, and $(3\,1\,1)$ surfaces of $CoCr_{2-y}Sc_yO_4$ were investigated using DFT/PBE0 formalism with an atom-centered basis set. The chemical environment of the most stable surface terminations for each investigated plane is depicted in Fig. 7, highlighting the existence of $[CrO_n]$ and $[ScO_n]$ clusters on the surface.

The $(3\,1\,1)$ surface is the most stable surface for a sizeable thermo-dynamic region in the phase diagram, exposing $[CrO_5]$, $[ScO_3]$, and $[CoO_2]$ clusters. Moreover, the $(1\,1\,0)$ and $(1\,1\,1)$ become more stable for the Co-poor environment. In this case, the first one exposed $[ScO_3]$ and $[CrO_3]$ clusters, while the $(1\,1\,1)$ surface plane exhibits similar clusters with the presence of $[CoO_2]$. On the other hand, the $(1\,0\,0)$ surface showed the smallest stable region in phase-diagram showing $[CrO_5]$, $[ScO_5]$, and $[CoO_2]$ exposed clusters. Based on the calculated surface energy values, different morphologies were proposed by $CoCr_2O_4$ NPs. It is worth mentioning that for the Co-poor region, a corner-truncated octahedral shape was found for the Cr-rich region, exposing the significant extent of $(1\,1\,1)$ and $(1\,1\,0)$ surfaces with a minor contribution from $(1\,0\,0)$, changing for a cubic-truncated and corner-truncated icosahedral shape moving to a poor Cr-region with the control of surface exposure for $(1\,1\,0)$ surface. Further, for intermediary and rich Co-composition, a generally rhombic shape containing a significant extent of $(3\,1\,1)$ surface with a minor contribution of other planes was found, following the

experimental data reported combining TEM and SAED patterns (Fig. 2).

The major aspect of such analysis depends on the surface spin density (D_μ) for $CoCr_{2-y}Sc_yO_4$ models that enables the calculation of magneti-zation index (M) for the obtained morphologies, as reported in Table 3. Comparing the spin density before and after Sc-doping, the obtained results indicate that $(1\,0\,0)$ and $(1\,1\,1)$ surfaces showed increased surface magnetism, while $(1\,1\,0)$ and $(3\,1\,1)$ exhibits reduced spin density values. Moreover, for $(3\,1\,1)$ surface, the reduced spin density is associated with the reduced numbers of exchange interactions in the exposed surfaces, once the isoelectronic replacement of Cr^{3+} by non-magnetic Sc^{3+} in-duces a stronger magnetic A-B site interaction resulting in an antipar-allel arrangement.

Furthermore, the reduced spin density for $(3\,1\,1)$ and $(1\,1\,0)$ surfaces induces a shape-selective control of the nanomagnetism for Sc-doped $CoCr_2O_4$ particles. In particular, the $(3\,1\,1)$-based shape dominates the phase diagram showing reduced uncompensated spins, contributing to tailor the magnetic properties of $CoCr_{2-y}Sc_yO_4$ NPs.

4. Conclusions

The magneto-structural properties of $CoCr_{2-y}Sc_yO_4$ NPs were studied in detail from experimental and theoretical efforts. The spinel cubic structure was confirmed for all samples, exhibiting a unit cell expansion resulting from the local structural disorder associated with the larger ionic radius for Sc^{3+}. The morphological analysis combined with Wulff construction confirmed the non-regular shape of the obtained samples, enclosing the $(3\,1\,1)$, $(1\,1\,0)$, and $(1\,1\,1)$ planes. Experimental and theo-retical results indicate two magnetic transitions at T_c and T_s, where the transition temperature decreases with an increase in Sc^{3+} concentration, confirming the magneto-structural behavior associated with the
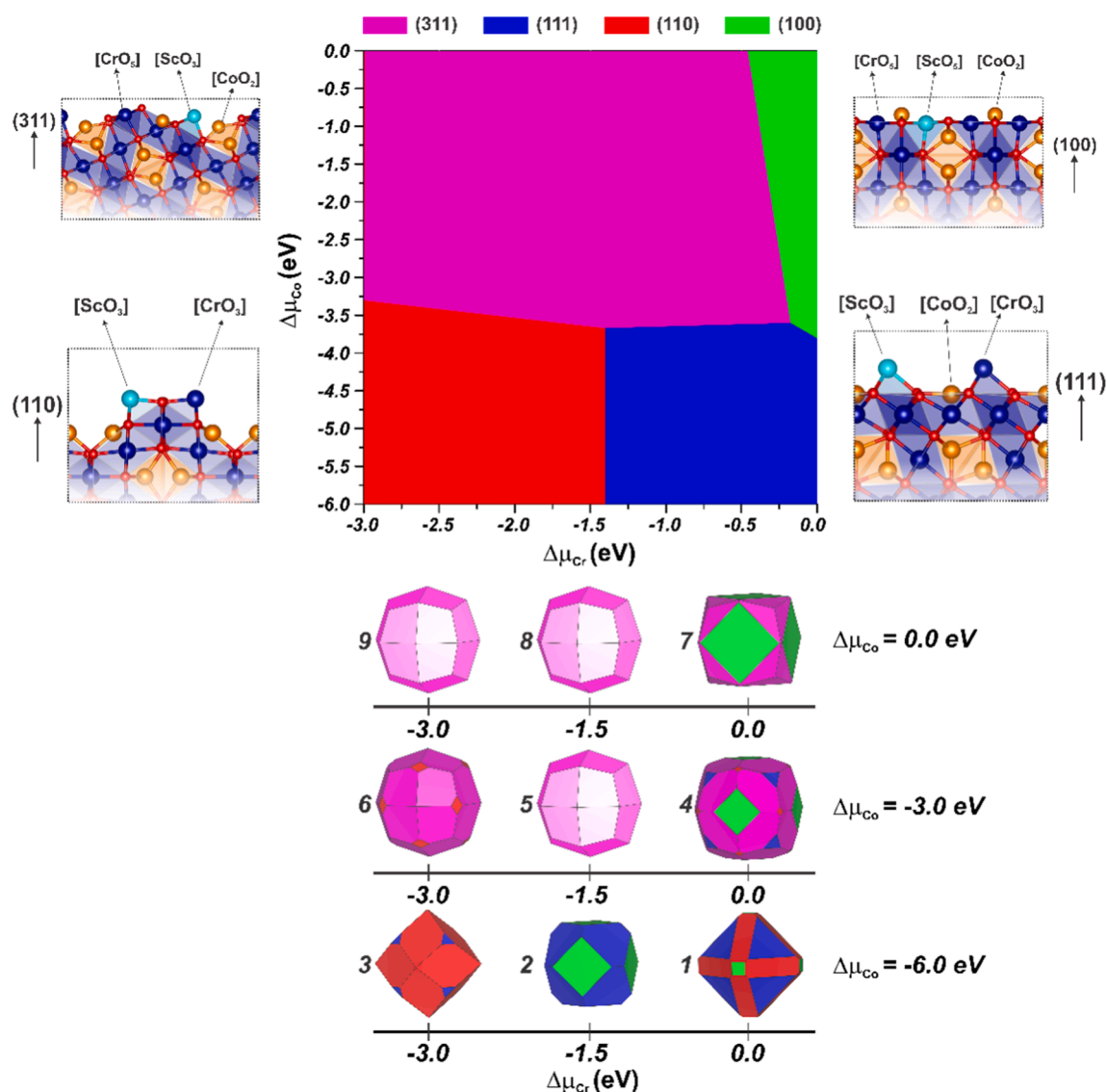
Fig. 7. Surface phase diagram and chemical environment for (1 0 0), (1 1 0), (1 1 1), and (3 1 1) surfaces of CoCr$_{2-y}$Sc$_y$O$_4$. Adapted from Ref. [32] with permission from The Royal Society of Chemistry.

Table 3

Spin density (D$_\mu$) and Magnetization index (M) for the pure and Sc-doped CoCr$_2$O$_4$ surfaces.

Surface	D$_\mu$ (μ_B nm^{-2})	
	Pure	Sc-doped
(1 0 0)	11.27	14.52
(1 1 0)	16.25	14.11
(1 1 1)	6.55	8.19
(3 1 1)	12.71	1.96
Morphologies	M values	
1	12.05	11.69
2	13.38	12.63
3	15.92	13.90
4	12.25	4.49
5	12.75	2.13
6	12.87	2.51
7	11.92	8.82
8	12.71	1.96
9	12.71	1.96

octahedral B-site doping, as confirmed by calculated exchange-coupling constants. The coercivity and remanent magnetization values decrease with an increase in Sc^{3+} concentration, following the spin density values calculated for (3 1 1) surface that induces an overall control of shape-selective nanomagnetism for CoCr$_2$O$_4$ NPs.

CRediT authorship contribution statement

V. Jagadeesha Angadi: Conceptualization, Methodology, Investigation, Writing – review & editing, Project administration. **K. Manjunatha:** Conceptualization, Methodology, Investigation, Data curation, Writing – review & editing. **Marisa C. Oliveira:** Conceptualization, Formal analysis, Investigation, Writing – review & editing, Visualization. **Elson Longo:** Writing – review & editing, Visualization, Funding acquisition. **Sergio R. de Lázaro:** Writing – review & editing, Visualization, Funding acquisition. **Renan A.P. Ribeiro:** Conceptualization, Investigation, Writing – review & editing, Visualization, Supervision, Project administration. **S.V. Bhat:** Writing – review & editing, Visualization, Supervision, Project administration.

Declaration of Competing Interest

The authors declare that they have no known competing financial interests or personal relationships that could have appeared to influence the work reported in this paper.

Acknowledgements

Appendix A. Supplementary material

Supplementary data to this article can be found online at https://doi.org/10.1016/j.apsusc.2021.151555.

References

[1] K. Nadeem, H.U. Rehman, F. Zeb, E. Ali, M. Kamran, N.A. Noshahi, H. Abbas, Magnetic phase diagram and dielectric properties of Mn doped $CoCr_2O_4$ nanoparticles, J. Alloys Compd. 832 (2020), 155031.

[2] A. Dashora, M. Suthar, K. Kumar, R.J. Choudhary, D.M. Phase, H. Sakurai, N. Tsuji, Y. Sakurai, B.L. Ahuja, Study of magnetism in Fe doped $CoCr_2O_4$ using magnetic Compton scattering and first-principles computations, J. Alloys Compd. 824 (2020), 153883.

[3] R.Z. Rasool, K. Nadeem, M. Kamran, F. Zeb, N. Ahmad, M. Mumtaz, Comparison of anomalous magnetic properties of non-collinear $CoCr_2O_4$ and $NiCr_2O_4$ nanoparticles, J. Magn. Magn. Mater. 514 (2020), 167225.

[4] M.S. Tomar, S.P. Singh, O. Perales-Perez, R.P. Guzman, E. Calderon, C. Rinaldi-Ramos, Synthesis and magnetic behavior of nanostructured ferrites for spintronics, Microelectron. J. 36 (2005) 475–479.

[5] G. Jagadish Kumar, A. Banerjee, A.S.K. Sinha, Y. Su, K. Nemkovski, C. Rath, Cation distribution and magnetic properties of Zn-substituted $CoCr_2O_4$ nanoparticles, J. Appl. Phys. 123 (2018), 223905.

[6] K. Manjunatha, V. Jagadeesha Angadi, R. Rajaramakrishna, U. Mahaboob Pasha, Role of 5 mol% Mg-Ni on the Structural and Magnetic Properties of Cobalt Chromates Crystallites Prepared by Solution Combustion Technique, J. Supercond. Novel Magn. 33 (2020) 2861–2866.

[7] I. Matulkova, P. Holec, B. Pacakova, S. Kubickova, A. Mantlikova, J. Plocek, I. Nemec, D. Niznansky, J. Vejpravova, On preparation of nanocrystalline chromites by co-precipitation and autocombustion methods, Mater. Sci. Eng. B 195 (2015) 66–73.

[8] C.N.R. Rao, A. Sundaresan, R. Saha, Multiferroic and Magnetoelectric Oxides: The Emerging Scenario, J. Phys. Chem. Lett. 3 (16) (2012) 2237–2246.

[9] K. Manjunatha, V. Jagadeesha Angadi, K.M. Srinivasamurthy, S. Matteppanavar, V.K. Pattar, U. Mahaboob Pasha, Exploring the Structural, Dielectric and Magnetic Properties of 5 Mol% Bi^{3+}-Substituted $CoCr_2O_4$ Nanoparticles, J. Supercond. Novel Magn. 33 (2020) 1747–1757.

[10] K. Manjunatha, V. Jagadeesha Angadi, R.A.P. Ribeiro, E. Longo, M.C. Oliveira, M.R.D. Bomio, S.R. de Lázaro, S. Matteppanavar, S. Rayaprol, P.D. Babu, M. Pasha, Structural, electronic, vibrational and magnetic properties of Zn^{2+} substituted $MnCr_2O_4$ nanoparticles, J. Magn. Magn. Mater. 502 (2020) 166595.

[11] M. Akyol, İ. Adanur, A.O. Ayaş, A. Ekicibil, Magnetic field dependence of magnetic coupling in $CoCr_2O_4$ nanoparticles, Phys. B 525 (2017) 144–148.

[12] P. Mohanty, C.J. Sheppard, A.R.E. Prinsloo, W.D. Roos, L. Olivi, G. Aquilanti, Effect of cobalt substitution on the magnetic properties of nickel chromite, J. Magn. Magn. Mater. 451 (2018) 20–28.

[13] D. Zákutná, A. Repko, I. Matulková, D. Nižňanský, A. Ardu, C. Cannas, A. Mantlíková, J. Vejpravová, Hydrothermal synthesis, characterization, and magnetic properties of cobalt chromite nanoparticles, J. Nanopart. Res. 16 (2014) 2251.

[14] A. Rathi, P.D. Babu, P.K. Rout, V.P.S. Awana, V.K. Tripathi, R. Nagarajan, B. Sivaiah, R.P. Pant, G.A. Basheed, Anomalous nano-magnetic effects in non-collinear spinel chromite $NiCr_2O_4$, J. Magn. Magn. Mater. 474 (2019) 585–590.

[15] P. Mohanty, A.M. Venter, C.J. Sheppard, A.R.E. Prinsloo, Structure and magnetic phase transitions in $(Ni_{1-x}Co_x)Cr_2O_4$ spinel nanoparticles, J. Magn. Magn. Mater. 498 (2020), 166217.

[16] C. Rath, P. Mohanty, Magnetic Phase Transitions in Cobalt Chromite Nanoparticles, J. Supercond. Novel Magn. 24 (2011) 629–633.

[17] C. Rath, P. Mohanty, A. Banerjee, Magnetic properties of nanoparticles of cobalt chromite, J. Magn. Magn. Mater. 323 (2011) 1698–1702.

[18] M. Ptak, M. Mączka, K. Hermanowicz, A. Pikul, J. Hanuza, Particle size effects on the magnetic and phonon properties of multiferroic $CoCr_2O_4$, J. Solid State Chem. 199 (2013) 295–304.

[19] Z. Tian, C. Zhu, J. Wang, Z. Xia, Y. Liu, S. Yuan, Size dependence of structure and magnetic properties of $CoCr_2O_4$ nanoparticles synthesized by hydrothermal technique, J. Magn. Magn. Mater. 377 (2015) 176–182.

[20] X. Chen, Z. Yang, Y. Xie, Z. Huang, L. Ling, S. Zhang, L. Pi, Y. Sun, Y. Zhang, Coexistence of incommensurate and commensurate spiral orders and pressure effect on polycrystalline $CoCr_2O_4$, J. Appl. Phys. 113 (2013) 17E129.

[21] R. Kumar, S. Rayaprol, V. Siruguri, Y. Xiao, W. Ji, D. Pal, Magneto-structural correlation in $Co_{0.8}Cu_{0.2}Cr_2O_4$ cubic spinel, J. Magn. Magn. Mater. 454 (2018) 342–348.

[22] D. Wang, M.F. Shu, L.H. Yin, X.W. Tang, P. Tong, X.B. Zhu, J. Yang, W.H. Song, Y.P. Sun, Substantially enhanced ferroelectricity in JT ion Cu^{2+}-doped $Co_{1-x}Cu_xCr_2O_4$ ($0 \le x \le 0.4$), Appl. Phys. Lett. 115 (2019), 082903.

[23] C.L. Li, T.Y. Yan, G.O. Barasa, Y.H. Li, R. Zhang, Q.S. Fu, X.H. Chen, S.L. Yuan, Negative magnetization and exchange bias effect in Fe-doped $CoCr_2O_4$, Ceram. Int. 44 (2018) 15446–15452.

[24] R. Kumar, S.K. Upadhyay, Y. Xiao, W. Ji, D. Pal, Influence of Fe substitution on multiferrocity and magneto-dielectric properties in $CoCr_2O_4$, J. Phys. D: Appl. Phys. 51 (2018), 385001.

[25] D. Kumar, K. Nemkovski, Y. Su, C. Rath, Enhancement of Curie- and spin-spiral temperatures with doping Fe in multiferroic $CoCr_2O_4$ nanoparticles, J. Magn. Magn. Mater. 488 (2019), 165378.

[26] M.A. Kassem, A. Abu El-Fadl, A.M. Nashaat, H. Nakamura, Magnetic evolution from the superparamagnetism in nanospinel chromites $Cd_{1-x}Co_xCr_2O_4$ ($0 \le x \le 1.0$), J. Magn. Magn. Mater. 495 (2020), 165830.

[27] A. Abu El-Fadl, A.M. Nashaat, M.A. Kassem, Characterization of spinel-type $Cd_{1-x}Co_xCr_2O_4$ nanocrystals by a microwave-combustion synthesis, Mater. Res. Express 6 (2019) 1150–1157.

[28] M. Kamran, A. Ullah, S. Rahman, A. Tahir, K. Nadeem, M.A.U. Rehman, S. Hussain, Structural, magnetic, and dielectric properties of multiferroic $Co_{1-x}Mg_xCr_2O_4$ nanoparticles, J. Magn. Magn. Mater. 433 (2017) 178–186.

[29] D. Kumar, A. Banerjee, A. Mahmoud, C. Rath, Cation distribution dependent magnetic properties in $CoCr_{2-x}Fe_xO_4$ (x=0.1 to 0.5): EXAFS, Mossbauer and magnetic measurements, Dalton Trans. 46 (2017) 10300–10314.

[30] P. Choudhary, D. Varshney, Structural, vibrational and dielectric behavior of $Co_{1-x}M_xCr_2O_4$ (M = Zn, Mg, Cu and x=0.0, 0.5) spinel chromites, J. Alloys Compd. 725 (2017) 415–424.

[31] A. Chatterjee, J.K. Dey, S. Majumdar, A.C. Dippe, O. Gutowski, M.V. Zimmermann, S. Giri, Tuning of multiferroic order with Co doping in $CuCr_2O_4$: Interplay between structure and orbital order, Phys. Rev. Mat. 3 (2019).

[32] K. Manjunatha, V.J. Angadi, M.C. Oliveira, S.R. de Lazaro, E. Longo, R.A.P. Ribeiro, S.O. Manjunatha, N.H. Ayachit, Towards shape-oriented Bi-doped $CoCr_2O_4$ nanoparticles from theoretical and experimental perspectives: structural, morphological, optical, electrical and magnetic properties, J. Mater. Chem. C 9 (2021) 6452–6469.

[33] K. Manjunatha, V.J. Angadi, R.A.P. Ribeiro, M.C. Oliveira, S.R. de Lázaro, M.R. D. Bomio, S. Matteppanavar, S. Rayaprol, P.D. Babu, U.M. Pasha, Structural, electronic and magnetic properties of Sc^{3+} doped $CoCr_2O_4$ nanoparticles, New J. Chem. 44 (2020) 14246–14255.

[34] R. Dovesi, A. Erba, R. Orlando, C.M. Zicovich-Wilson, B. Civalleri, L. Maschio, M. Rérat, S. Casassa, J. Baima, S. Salustro, B. Kirtman, Quantum-mechanical condensed matter simulations with CRYSTAL, Wiley Interdiscip, Rev.: Comput. Mol. Sci. 8 (4) (2018), https://doi.org/10.1002/wcms.2018.8.issue-410.1002/wcms.1360.

[35] C. Adamo, V. Barone, Toward reliable density functional methods without adjustable parameters: The PBE0 model, J. Chem. Phys. 110 (13) (1999) 6158–6170.

[36] R.I. Eglitis, J. Purans, J. Gabrusenoks, A.I. Popov, R. Jia, Comparative Ab Initio Calculations of ReO_3, $SrZrO_3$, $BaZrO_3$, $PbZrO_3$ and $CaZrO_3$ (001) Surfaces, Crystals 10 (2020) 745.

[37] R.I. Eglitis, A.I. Popov, Systematic trends in (001) surface ab initio calculations of ABO_3 perovskites, J. Saudi Chem. Soc. 22 (2018) 459–468.

[38] R.A.P. Ribeiro, S.R. de Lazaro, C. Gatti, The role of exchange–correlation functional on the description of multiferroic properties using density functional theory: the $ATiO_3$ (A = Mn, Fe, Ni) case study, RSC Adv. 6 (2016) 101216–101225.

[39] H. Guo, A.C. Marschilok, K.J. Takeuchi, E.S. Takeuchi, P. Liu, Rationalization of diversity in spinel $MgFe_2O_4$ surfaces, Adv. Mater. Interfaces 6 (2019) 1901218.

[40] H. Guo, A.C. Marschilok, K.J. Takeuchi, E.S. Takeuchi, P. Liu, Essential role of spinel $ZnFe_2O_4$ surfaces during lithiation, ACS Appl. Mater. Interfaces 10 (2018) 35623–35630.

[41] R. Cristina de Oliveira, R.A. Pontes Ribeiro, G.H. Cruvinel, R.A. Ciola Amoresi, M.H. Carvalho, A.J. Aparecido de Oliveira, M. Carvalho de Oliveira, S. Ricardo de Lazaro, L. Fernando da Silva, A.C. Catto, A.Z. Simões, J.R. Sambrano, E. Longo, Role of surfaces in the magnetic and ozone gas-sensing properties of $ZnFe_2O_4$ nanoparticles: theoretical and experimental insights, ACS Appl Mater. Interfaces 13 (3) (2021) 4605–4617.

[42] K. Reuter, M. Scheffler, Composition and structure of the RuO_2 (110) surface in an O_2 and CO environment: Implications for the catalytic formation of CO_2, Phys. Rev. B 68 (2003), 045407.

[43] E. Heifets, S. Piskunov, E.A. Kotomin, Y.F. Zhukovskii, D.E. Ellis, Electronic structure and thermodynamic stability of double-layered $SrTiO_3$ (001) surfaces: Ab initio simulations, Phys. Rev. B 75 (2007), 115417.

[44] R.E. Warburton, H. Iddir, L.A. Curtiss, J. Greeley, Thermodynamic stability of low- and high-index spinel $LiMn_2O_4$ surface terminations, ACS Appl. Mater. Interfaces 8 (17) (2016) 11108–11121.

[45] S. Kim, M. Aykol, C. Wolverton, Surface phase diagram and stability of (001) and (111) $LiMn_2O_4$ spinel oxides, Phys. Rev. B 92 (2015), 115411.

[46] A.A.G. Santiago, R.L. Tranquilin, M.C. Oliveira, R.A.P. Ribeiro, S.R. de Lazaro, M. A. Correa, F. Bohn, E. Longo, F.V. Motta, M.R.D. Bomio, Disclosing the structural, electronic, magnetic, and morphological properties of $CuMnO_2$: a unified experimental and theoretical approach, J. Phys. Chem. C (2020).

[47] R.A.P. Ribeiro, J. Andrés, E. Longo, S.R. Lazaro, Magnetism and multiferroic properties at $MnTiO_3$ surfaces: A DFT study, Appl. Surf. Sci. 452 (2018) 463–472.

[48] R.A.P. Ribeiro, S.R. de Lazaro, L. Gracia, E. Longo, J. Andrés, Theoretical approach for determining the relation between the morphology and surface magnetism of Co_3O_4, J. Magn. Magn. Mater. 453 (2018) 262–267.

[49] R.A.P. Ribeiro, L.H.S. Lacerda, E. Longo, J. Andrés, S.R. de Lazaro, Towards enhancing the magnetic properties by morphology control of $ATiO_3$ (A = Mn, Fe, Ni) multiferroic materials, J. Magn. Magn. Mater. 475 (2019) 544–549.

[50] H.J. Monkhorst, J.D. Pack, Special points for Brillouin-zone integrations, Phys. Rev. B 13 (1976) 5188–5192.

[51] E. Ruiz, M. Llunell, P. Alemany, Calculation of exchange coupling constants in solid state transition metal compounds using localized atomic orbital basis sets, J. Solid State Chem. 176 (2003) 400–411.

[52] R. Dovesi, F. Freyria Fava, C. Roetti, V.R. Saunders, Structural, electronic and magnetic properties of KMF_3 (M=Mn, Fe Co, Ni), Faraday Discuss. 106 (1997) 173–187.

[53] A.M. Ferrari, C. Pisani, An ab Initio Periodic Study of NiO Supported at the Pd(100) Surface. Part 1: The Perfect Epitaxial Monolayer, J. Phys. Chem. B 110 (2006) 7909–7917.

[54] T. Bredow, K. Jug, R.A. Evarestov, Electronic and magnetic structure of $ScMnO_3$, Phys. Status Solidi B 243 (2) (2006) R10–R12.

[55] K. Tomiyasu, J. Fukunaga, H. Suzuki, Magnetic short-range order and reentrant-spin-glass-like behavior in $CoCr_2O_4$ and $MnCr_2O_4$ by means of neutron scattering and magnetization measurements, Phys. Rev. B 70 (2004), 214434.

[56] A.V. Pronin, M. Uhlarz, R. Beyer, T. Fischer, J. Wosnitza, B.P. Gorshunov, G. A. Komandin, A.S. Prokhorov, M. Dressel, A.A. Bush, V.I. Torgashev, B-T phase diagram of $CoCr_2O_4$ in magnetic fields up to 14 T, Phys. Rev. B 85 (2012), 012101.

[57] V.J. Angadi, K. Manjunatha, M. Akyol, A. Ekicibil, S. Matteppanavar, A. V. Pavlenko, S.P. Kubrin, Temperature-dependent dielectric and magnetic properties of scandium-substituted $HoFeO_3$ nanoparticles, J. Supercond. Novel Magn. 33 (2020) 3525–3534.

[58] R.N. Bhowmik, R. Ranganathan, Lattice expansion and noncollinear to collinear ferrimagnetic order in a $MnCr_2O_4$ nanoparticle, Phys. Rev. B 73 (2006), 144413.

[59] D. Kumar, G.C. Pandey, A. Banerjee, A. Mahmoud, C. Rath, Effect of Fe substitution on the cation distribution and magnetic properties of $CoCr_{2-x}Fe_xO_4$ (x = 0.6 to 1.0) nanoparticles, J. Phys. Chem. Solids 148 (2021), 109590.

[60] D.H. Lyons, T.A. Kaplan, K. Dwight, N. Menyuk, Classical theory of the ground spin-state in cubic spinels, Phys. Rev. 126 (1962) 540–555.